ACS APPLIED MATERIALS & INTERFACES

Research Article

Cite This: ACS Appl. Mater. Interfaces 2018, 10, 31552−31559

www.acsami.org

Analysis of the Bias-Dependent Split Emission Zone in Phosphorescent OLEDs

Markus Regnat,*[,†,‡] Kurt P. Pernstich,[†] Simon Züfle,[†,§] and Beat Ruhstaller[†,§]

[†]Institute of Computational Physics, Zurich University of Applied Sciences (ZHAW), Technikumstrasse 9, 8400 Winterthur, Switzerland

[‡]Institut des Matériaux, Ecole Polytechnique Fédérale de Lausanne, EPFL, Station 12, 1015 Lausanne, Switzerland

[§]Fluxim AG, Katharina-Sulzer-Platz 2, 8400 Winterthur, Switzerland

Supporting Information

ABSTRACT: From s-polarized, angle-dependent measurements of the electroluminescence spectra in a three-layer phosphorescent organic light-emitting diode, we calculate the exciton distribution inside the 35 nm thick emission layer. The shape of the exciton profile changes with the applied bias due to differing field dependencies of the electron and hole mobilities. A split emission zone with high exciton densities at both sides of the emission layer is obtained, which is explained by the presence of energy barriers and similar electron and hole mobilities. A peak in the transient electroluminescence signal after turn-off and the application of a reverse bias is identified as a signature of a split emission zone.

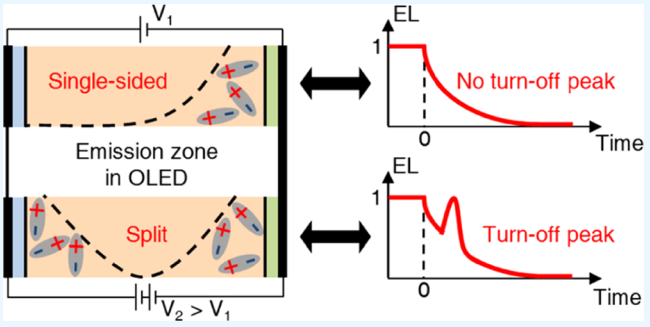

KEYWORDS: *OLED, emission zone, exciton profile, angle-dependent electroluminescence spectra, transient electroluminescence decay*

INTRODUCTION

Organic light-emitting diodes (OLEDs) nowadays reach high external quantum efficiencies of 30% and above,[1−5] and they are commonly used in displays for smartphones, televisions, and increasingly as lighting elements. In general, a high luminance is desired, which can be achieved with high current densities. However, this driving condition often causes a reversible decrease of the efficiency.[6,7] To optimize the layer stack for maximum light output, the knowledge of the emission zone (EMZ) inside the emission layer (EML) is essential. The location and extent of the emission zone are closely related to the current balance, i.e., where the charges accumulate and recombine both radiatively and nonradiatively, which limits the quantum efficiency of the OLED. Exciton confinement inside the EML is thus a key factor in optimizing OLED efficiency.[8−10] The EMZ generally depends on the driving current and on the state of degradation, and it is affected by exciton quenching mechanisms if present.

Different techniques have been used to provide information about the emission zone, namely, the use of sensing layers,[8,11−17] electro-optical simulations,[11,18−23] and measuring and modeling the angle-dependent electroluminescence (EL).[24−29] In this work, we use the latter two techniques to investigate the changes in the EMZ with increasing current densities. Our findings reveal that the emission zone has two peaks at either side of the emission layer, and the maximum of this split emission zone shifts with the applied bias. This split emission zone gives rise to an EL peak after the OLED is turned-off and reverse-biased where the peak height depends on the forward voltage. To elucidate the EMZ from optical measurements, the OLED cavity has to be optically detuned to maximize the sensitivity of the angle-dependent signal to changes of the EMZ rather than to maximize the light output. The peak in the transient EL decay is also observed in an OLED stack optimized for light output, highlighting that split emission zones can be a general feature in OLEDs. With bottom-up electro-optical simulations of an idealized OLED stack, the finding of a split emission zone is directly linked with the appearance of the peak in the EL signal after turn-off.

RESULTS AND DISCUSSION

The bottom-emission OLED stack under investigation is shown in Figure 1 and comprises indium tin oxide (ITO, 100 nm)/poly(3,4-ethylenedioxythiophene):polystyrene sulfonate (PEDOT:PSS, 30 nm)/4,4′,4″-tris(carbazol-9-yl)-triphenylamine (TCTA, 46 nm)/4,4′-bis(carbazol-9-yl)-biphenyl (CBP):bis(2-phenylpyridine)(acetylacetonate)-iridium(III) ($Ir(ppy)_2(acac)$, 35 nm, 5 wt %)/2,9-bis-(naphthalen-2-yl)-4,7-diphenyl-1,10-phenanthroline (NBPhen, 52 or 120 nm)/Ca (15 nm)/Al (100 nm). The thickness of the NBPhen electron transport layer (ETL) of 52 nm in the optically tuned OLED maximizes the light output. To

Received: June 8, 2018
Accepted: August 27, 2018
Published: August 27, 2018

DOI: 10.1021/acsami.8b09595
ACS Appl. Mater. Interfaces 2018, 10, 31552−31559

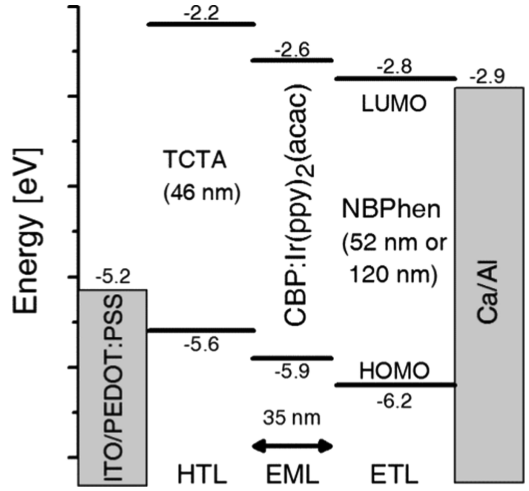

Figure 1. Energy-level diagram of the fabricated OLEDs. The emission layer is only 35 nm thin, and the thickness of the NBPhen layer is either 52 nm in the tuned OLED or 120 nm in the optically detuned OLED.

determine the emission zone in the thin EML from optical measurements, the ETL thickness was increased to 120 nm in the optically detuned OLED. The optical detuning maximizes the sensitivity of the angle-dependent s-polarized EL spectra to changes in the emission zone[30,31] and reduces the measured current efficiency by a factor of 40. The thickness of the TCTA hole transporting layer (HTL) was kept constant, as its influence on the angular emission is minor.

Split Emission Zone. Figure 2a shows the measured and simulated EL spectra for various angles at an intermediate current of 0.5 mA together with the photoluminescence (PL) spectrum of the $Ir(ppy)_2(acac)$ dopant; Figure S1 shows the spectra at 0.1 and 4 mA. The excellent agreement over the entire wavelength and viewing angle range was obtained with the emission zones shown in Figure 2c. For a constant current density, the EL spectrum changes with the viewing angle because the interference effect in the OLED cavity evolves with the viewing angle. For low angles, a peak near 520 nm is present, whereas at larger angles, a second resonance appears in the EL spectrum near 570 nm. Consequently, the long-wavelength shoulder in the PL spectrum (Figure 2a) of the emitting species is pronounced at 70°. The evolution of the EL spectrum with current is shown in Figure 2b for a fixed angle of 30°. The long-wavelength shoulder at around 570 nm in the normalized spectrum nearly vanishes for increasing currents. This measured intensity decrease at 570 nm for increasing currents has to be associated with changes in the spatial distribution of the exciton density inside the EML and is, thus, a clear evidence that the emission zone changes with current.

The emission zones calculated from angle-dependent measurements at all three current densities are shown in Figure 2c. High exciton densities are present at both interfaces of the EML. A split emission zone has also been reported in refs 23 and 32, whereas other OLED stacks can also show homogeneous or single-sided emission zones as reported in, e.g. refs 12 and 13. Having high emission at both EML interfaces indicates the presence of high electron and hole concentrations at both interfaces. This somewhat counter-intuitive observation can easily be rationalized by the presence of energy barriers for holes at the EML/ETL interface and for electrons at the HTL/EML interface, as illustrated in Figure 3b. Without these energy barriers, no confinement of the unrecombined electrons and holes inside the EML takes place, and instead of forming a split emission zone, the leakage currents would increase, thus reducing the internal quantum efficiency. Electrical simulations of an idealized OLED further support and illustrate this explanation as discussed below.

The exciton distributions in Figure 2c show that the position of the highest emission intensity shifts from the EML/ETL to the HTL/EML interface for increasing current densities. A similar shift of the exciton density with current was observed by Coburn et al.[12] in $mCBP:Ir(dmp)_3$ OLEDs by using sensing layers. At an intermediate current of 0.5 mA, the exciton densities at both interfaces are equal and the emission zone is balanced. As discussed in detail below, this balance leads to the largest peak intensity in the transient EL signal when the OLED is reverse-biased. We note that the observed shift of the emission zone maxima is caused by a different field dependence of the hole and the electron mobility, as discussed in the context of Figure 4.

Transient Electroluminescence. The biasing scheme for the transient electroluminescence measurements is illustrated in Figure 3a. After applying a certain forward voltage for a time long enough to reach a steady state, the OLED is reverse-

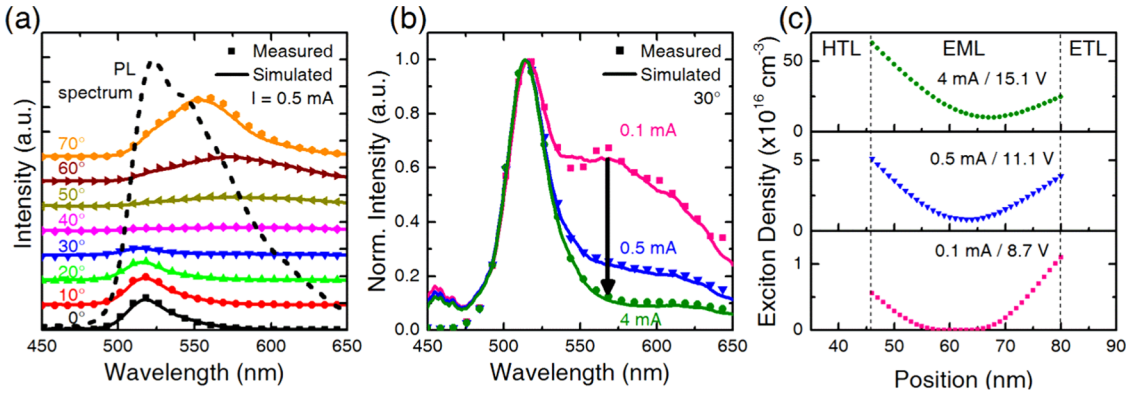

Figure 2. Measured (symbols) and simulated (solid lines) angle-dependent s-polarized EL spectra for a constant current of 0.5 mA together with the PL spectrum of the Ir(ppy)2(acac) dopant (a). (b) EL spectra at an angle of 30° for different currents. The shoulder at 570 nm is reduced significantly for increasing currents proving that the emission zone is changing with current. From these measurements, the optical model yields the emission zones shown in (c).

DOI: 10.1021/acsami.8b09595
ACS Appl. Mater. Interfaces 2018, 10, 31552−31559

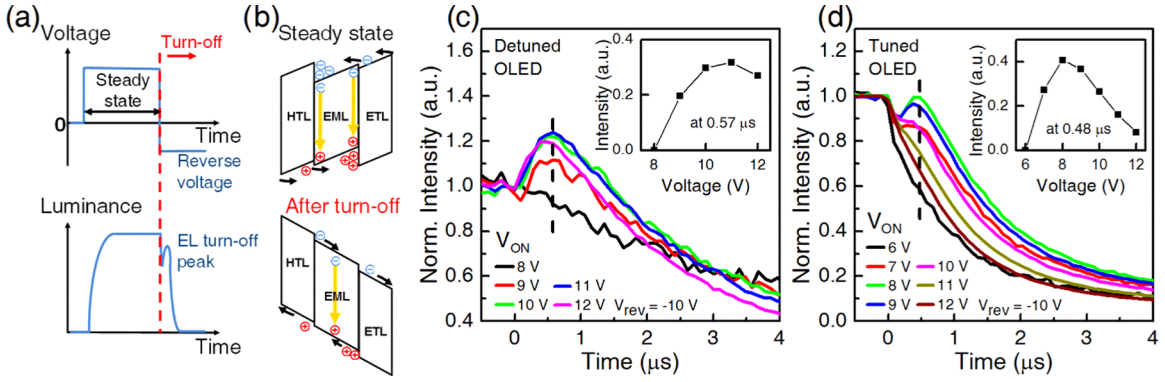

Figure 3. (a) Biasing scheme for the transient electroluminescence measurements. (b) Illustration of the energy diagram highlighting the accumulation of excess electrons at the HTL/EML and of excess holes at the EML/ETL interface that drift toward each other under reverse bias, which leads to an increased recombination and the observed EL peak in detuned (c) and tuned (d) OLEDs. The insets show that this peak intensity increases with on-voltage up to a certain voltage before it decreases.

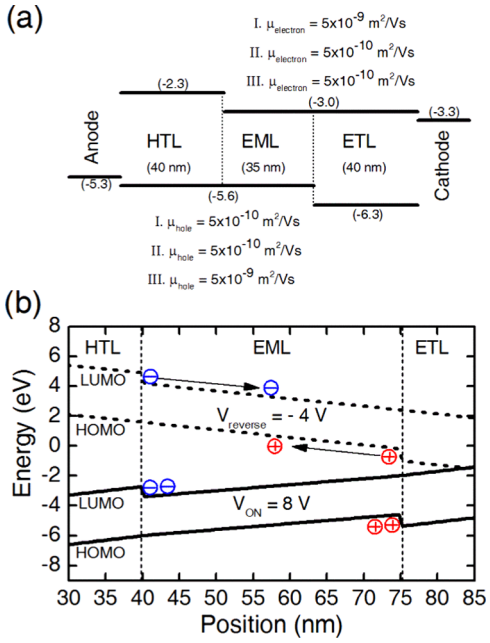

Figure 4. (a) Energy levels and mobility values used in the idealized model of a tuned OLED for cases I–III. The band diagram in (b) illustrates the accumulation of excess electrons and holes at the respective EML interfaces at steady state. After reverse-biasing, these excess electrons and holes migrate toward the center, where they can generate additional excitons, which leads to the observed peak in the transient EL signal.

biased with −10 V while the EL signal is measured. On top of the expected EL decay, a peak is observed that is caused by the split emission zone, as shown in Figure 3c for the detuned OLED. This peak exceeds the steady-state value for voltages higher than 8 V. The peak appears approx. 0.5 μs after turn-off, and its intensity scales with on-voltages up to 11 V, before it decreases for larger forward voltages, as shown in the inset to Figure 3c. The schematic energy diagram in Figure 3b illustrates the mechanism leading to this turn-off peak. Due to energy barriers between the EML and the neighboring HTL and ETL layers, electrons and holes that did not form excitons due to the low minority carrier density accumulate at the HTL/EML and the EML/ETL interface, respectively. This leads to the observed split emission zone and to the turn-off peak because these excess charge carriers drift toward each other upon applying the reverse bias and recombine when those charge carrier clouds meet. Without energy barriers at both EML interfaces, the leakage current would increase and no turn-off peak would be observed. The occurrence of a turn-off peak in the EL decay signal in reverse-biased OLEDs is, thus, a clear signature of a split emission zone. A turn-off peak has also been observed in, e.g., refs 33 and 34, but without reporting a dependence on the emission zone profile and on driving conditions.

To demonstrate that a split emission zone can also be present in optimized OLEDs with maximized emission intensity, the transient EL signals of a tuned OLED are shown in Figure 3d. As in the detuned OLED, the same trend of the turn-off peak with an increasing intensity up to a certain on-voltage (V_{on}) is observed. As shown in the inset of Figure 3d, the maximum peak intensity occurs at a lower on-voltage of 8 V compared to 11 V for the detuned OLED because the voltage to reach the same ratio of excess charges is lower in the tuned OLED due to the decreased resistance of the thinner ETL layer.[35,36] The average electric fields in the tuned OLED for 8 V and in the detuned OLED for 11 V are similar (55 and 60 V/μm), confirming the consistent behavior of the two OLEDs. Because the turn-off peak in transient EL measurements under reverse bias is also present in tuned OLEDs, we argue that the presence of such an EL turn-off peak is in general a signature of a split emission zone.

Electrical Simulations of an Idealized OLED. To further support the identification of the split emission zone from optical and transient EL measurements, we devised an electrical model for an idealized OLED stack. This illustrative example shows the requirements for the occurrence of a split emission zone, explains the observed EL turn-off peak, and sheds light on the physical mechanisms at work. The idealized OLED consists of the same three layers as in the measured devices, but energy levels have been adapted to be aligned, except for the lowest unoccupied molecular orbital (LUMO) levels at the HTL/EML interface and for the highest occupied molecular orbital (HOMO) levels at the EML/HTL interface, as illustrated in Figure 4a. The model employs either a constant (cases I–III in Figure 5) or a field-dependent mobility model (case IV in Figure 6) to simulate the electronic and optical properties. To account for the high exciton densities at certain bias conditions, triplet–polaron quenching (TPQ) and triplet–triplet annihilation (TTA) have been investigated but showed no relevant effect on the formation of

DOI: 10.1021/acsami.8b09595
ACS Appl. Mater. Interfaces 2018, 10, 31552–31559

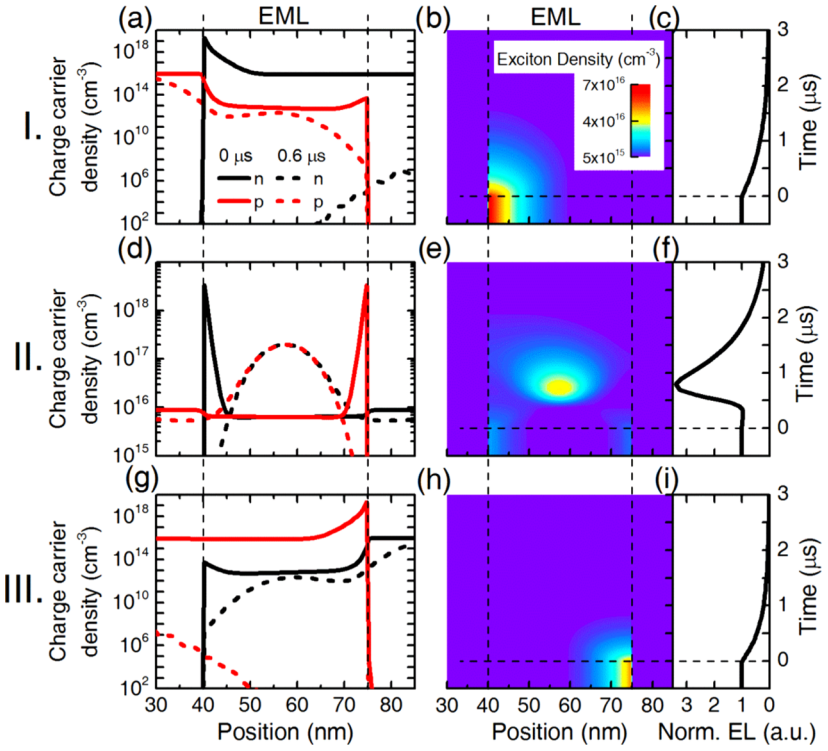

Figure 5. Charge carrier profiles at 0 and 0.6 μs after turn-off (a, d, g); temporal evolution of the emission zone (b, e, h); and resulting EL signal (c, f, i) for the three different electron and hole mobility combinations (cases I–III) in the ideal OLED. Under reverse bias, the excess charge carriers migrate toward the electrodes. In cases I and III, no excess minority charge carrier is present and the electroluminescence decays without a peak, whereas in case II, excess holes and electrons, present at both interfaces of the EML, form a significant number of excitons, which leads to the peak in the transient EL signal.

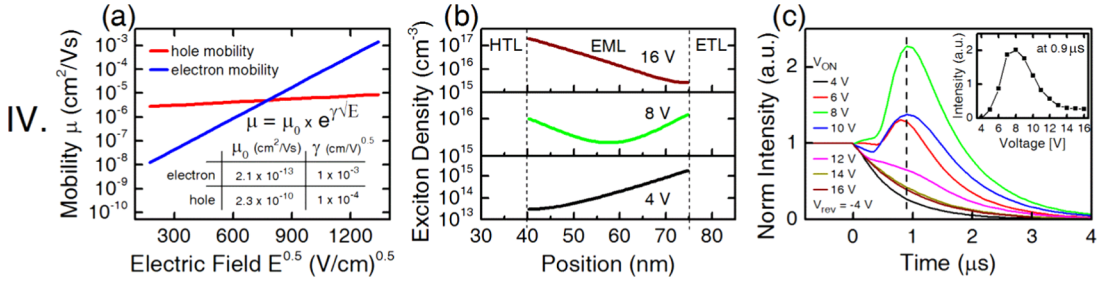

Figure 6. Electron and hole mobilities used in the simulation plotted for typical electric fields (a) and simulated exciton densities for different biases (b). At an applied voltage of 8 V where both mobilities are equal, the split emission zone shows nearly balanced exciton densities at both EML interfaces, which results in the largest turn-off peak in the simulated transient EL signal (c).

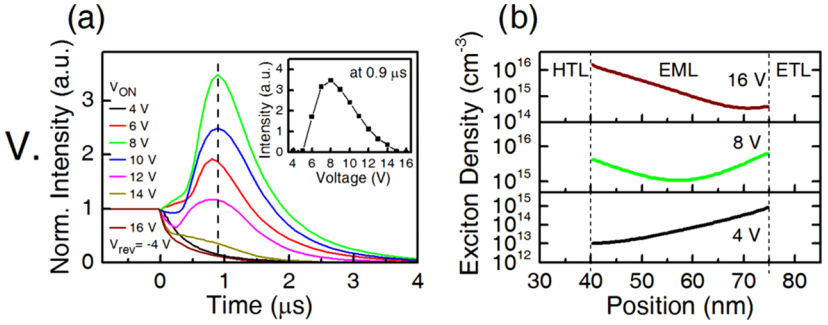

Figure 7. Transient EL signal (a) and exciton densities (b) when triplet–polaron quenching is considered in the model. The same qualitative results as those without quenching were obtained.

a split emission zone, as discussed in case V (Figure 7) and VI (Figure S2).

Figure 4b shows the modeled energy-band diagram in steady state under forward bias and right after applying a reverse bias of −4 V for equal electron and hole mobilities (case II). Under

DOI: 10.1021/acsami.8b09595
ACS Appl. Mater. Interfaces 2018, 10, 31552–31559

forward bias, electrons and holes accumulate at the respective interface of the EML due to the presence of an energy barrier of 700 meV. Not all charge carriers form excitons due to the low minority carrier density, as discussed in detail below, and the excess charge carriers drift toward each other under reverse bias conditions, as illustrated in Figure 4b. When those excess charge carrier clouds meet, they generate additional excitons that recombine and cause a peak in the transient EL signal after turn-off (c.f. Figure 5d–f). In the case of exactly balanced electron and hole densities in the EML (at all voltages), no excess charge carriers would accumulate at the respective interfaces and thus there would likely be no turn-off peak.

The detailed charge carrier profiles at 0 and 0.6 μs after turn-off are shown in Figure 5a,d,g for different combinations of hole and electron mobilities (cases I–III). Figure 5b,e,h shows the temporal evolution of the emission zone at steady state and after turn-off, and Figure 5c,f,i shows the resulting EL signal normalized to the steady-state value under forward bias.

In case I (Figure 5a–c), the electron mobility in the EML and ETL is 10 times higher than the hole mobility in the EML and HTL, which leads to a larger electron than hole density (Figure 5a). After exciton formation, a large number of excess electrons remains due to the lower hole density. These excess electrons accumulate at the HTL/EML interface, and a single-sided emission zone is formed. We note that accumulation of electrons can extend into the HTL if the energy barrier is low, especially for a large electron mobility in the HTL. Upon applying a reverse bias, the excess electrons migrate toward the cathode, and because the hole density is much lower, the majority of electrons reach the cathode without forming excitons, whereas the holes migrate less due to the lower mobility. Therefore, the electroluminescence signal decays without a peak.

For case II in Figure 5d–f, the electron and hole mobilities are equal and the excess electron and hole densities are identical at both EML interfaces. This leads to a nearly balanced exciton distribution with equal number of excitons at either side of the EML. Due to the Purcell effect, which increases the exciton decay rate near the metal cathode, the maximum exciton density is slightly higher at the anode side of the EML, as can be seen in Figure 5e and by comparing Figure 5b,h. When the excess electrons and holes migrate toward the center of the EML under reverse bias (dotted lines in Figure 5d), a significant number of excitons are formed in the center of the EML (Figure 5e), leading to a pronounced peak in the transient electroluminescence (Figure 5f).

Case III (Figure 5g–i) is inverse to case I, and the higher hole mobility causes a higher hole than electron density in the EML, with excess holes at the EML/ETL interface. Under reverse bias, the excess holes migrate to the anode, and because there are no excess electrons, the electroluminescence decays without a peak.

The simulations for cases I–III demonstrate that an EL turn-off peak is observed only if a split emission zone is formed. The split emission zone is formed when electron and hole mobilities are equal or similar and energy barriers for electrons are present at the HTL/EML interface and for holes at the EML/ETL interface. The same behavior can be expected in nonideal devices as long as electron and hole injections into the EML are equal or similar.

To explain the measured bias-dependent emission zone, the simulations for case IV used a different field dependence of the electron and the hole mobility. We argue that only a different field dependence leads to the observed bias-dependent emission zone. Figure 6a shows the electron and hole mobilities for typical electric fields inside the OLED stack.[37,38] An electric field exists at which both mobilities are equal, as in case II above, due to the different field dependencies. At higher fields, the electron mobility is larger than the hole mobility (case I), whereas at lower fields, the situation is reversed (case III).

Figure 6b shows the exciton densities at three different voltages. At low external bias, the emission zone is located mainly at the EML/ETL interface, whereas at high bias, the maximum emission originates from the HTL/EML interface. At an intermediate bias, the exciton densities are nearly equal at both EML interfaces. This balanced and split emission zone leads again to the largest peak in the transient turn-off signal under reverse bias, as shown in Figure 6c. The inset to Figure 6c shows the peak height of this turn-off peak for different on-voltages. The same behavior as in the measurements (Figure 3c,d) is observed, confirming that the exciton density is split and balanced on both sides of the EML for a bias of 11 or 8 V for the detuned and tuned case, respectively. The different field-dependences of the electron and hole mobilities are, thus, responsible for the changing emission zone with the applied bias. If electron and hole mobilities had the same field dependence, the ratio of the effective mobilities at different biases would be equal and no bias-dependent change of the emission zone would occur. We note that the exact condition for the appearance of the largest peak is a complex interplay between the mobility values, especially their field dependence, the energy barriers, and the Purcell factor of the OLED cavity. Nevertheless, the maximum peak always occurs when the exciton density is nearly balanced at both EML interfaces.

The local charge carrier and exciton densities in the idealized OLEDs are in a range where triplet–polaron quenching (TPQ) or triplet–triplet annihilation (TTA) can become significant.[39] If these exciton quenching processes are considered in the simulations, the results remain qualitatively the same as shown for TPQ in Figure 7 and for TTA in Figure S2. The exciton quenching leads to a faster EL decay (Figures 7a and S2a), but the peak in the transient EL signal under reverse bias appears at the same time as in the case without quenching and the maximum peak height is again obtained for an on-voltage of 8 V as expected.

The emission zone for the case considering exciton quenching is again single-sided for low and for high applied bias and is nearly balanced for an intermediate voltage that results in the largest EL turn-off peak (see Figures 7a and S2a). In comparison to that in Figure 6c, the exciton density in Figure 7b is lower due to exciton quenching, especially at high biases. The peak height in Figure 7a with exciton quenching appears larger than in Figure 6c without quenching, but this is due to the large effect of TPQ in the steady state, which lowers the intensity used for normalization. The number of excess electrons and holes remains the same irrespective of exciton quenching mechanisms; thus, the number of additional excitons formed after turn-off remains essentially the same. Initial studies reveal a tendency that the measurements are better explained when exciton quenching mechanisms are included, and further studies are in progress to clarify the role of exciton quenching in those devices.

DOI: 10.1021/acsami.8b09595
ACS Appl. Mater. Interfaces 2018, 10, 31552–31559

CONCLUSIONS

We have shown how measurements of angle-dependent EL spectra in optically detuned OLEDs reveal changes in the spatial distribution of the exciton density with applied bias in three-layer phosphorescent OLEDs. The emission zone obtained by solving the inverse problem on the basis of a dipole emission model can have two peaks at either side of the emission layer, and the maximum of this split emission zone shifts with the applied bias due to differing field dependencies of the electron and hole mobilities. A large excess charge density at both sides of the emissive layer leads to a pronounced electroluminescence peak after the OLED is reverse-biased. The intensity of this turn-off peak depends on the extent of the split emission zone, and a bias dependence of the peak height implies changes of the split emission zone with forward voltage. Our findings are rationalized with electrical charge drift-diffusion device simulations and are largely unaffected by exciton quenching processes. The bias-dependent split emission zone can also be present in optimized OLEDs that maximize light output.

MATERIALS AND METHODS

OLED Fabrication. For the fabrication of OLEDs, we used commercially available glass substrates structured with a 20 Ω/sq indium tin oxide (ITO) from Ossila. After cleaning in acetone and isopropanol in an ultrasonic bath, a 15 min UV−ozone treatment was performed, directly followed by spin-coating poly(3,4-ethylenedioxythiophene):polystyrene sulfonate (PEDOT:PSS, Clevios P VP AI 4083) with a spin speed of 3000 rpm. Before evaporating the organic materials, the substrates were annealed for 10 min at 160 °C under a nitrogen atmosphere in a glove box. The phosphorescent OLED stack consists of ITO (100 nm)/PEDOT:PSS (30 nm)/TCTA (46 nm)/CBP:Ir(ppy)$_2$(acac) (35 nm, 5 wt %)/NBPhen (52 or 120 nm)/Ca (15 nm)/Al (100 nm). The organic materials 4,4′,4″-tris(carbazol-9-yl)triphenylamine (TCTA), 4,4′-bis(carbazol-9-yl)biphenyl (CBP), bis(2-phenylpyridine)(acetylacetonate)iridium(III) (Ir(ppy)$_2$(acac)), and 2,9-bis(naphthalen-2-yl)-4,7-diphenyl-1,10-phenanthroline (NBPhen) were purchased from Lumtec and were evaporated under high vacuum of $<10^{-6}$ mbar without any prior purification. TCTA was used as a hole transport layer (HTL) and electron-blocking layer due to its higher lowest unoccupied molecular orbital (LUMO) level than the CBP LUMO level. NBPhen was used as an electron transport layer (ETL), which has a good hole-blocking property due to its low-lying highest occupied molecular orbital (HOMO) compared to the HOMO level of CBP. The energy levels with values taken from the literature[19,40,41] are shown in Figure 1. The phosphorescent emitter Ir(ppy)$_2$(acac) was coevaporated with the CBP host to obtain a concentration of ≈5 wt %. For the evaporation of the Ca/Al cathode, the shadow masks were exchanged and the samples were exposed to N_2. After fabrication, the OLEDs were encapsulated using an encapsulation epoxy and a cover glass from Ossila under a nitrogen atmosphere. The optical and electrical characterization took place in air, and the active area of the OLED pixels is 0.045 cm^2.

EL Measurements. The angle-dependent s-polarized EL spectra were measured in a home-built setup consisting of a half cylinder lens and a rotational stage with a detector unit comprising pinhole, polarizer, retarder, and a ULS2048L spectrometer (Avantes). The angular measurement range is from −70 to +70° with respect to the surface normal, and with a 1 mm diameter pinhole an angular resolution of less than ±1° is achieved. The setup is connected with the all-in-one measurement system Paios from Fluxim,[42] and a redesigned version of the setup is now available as the angular luminescence spectrometer Phelos by Fluxim. The half cylinder lens out-couples all substrate modes to air and thus allows us to measure the entire angle-dependent EL spectra in the glass substrate. A gated Hamamatsu photosensor module (H11526-110) attached to Paios was used to measure the time-dependent EL decay.

Calculating the Emission Zone. To calculate the shape of the emission zone from measured angle-dependent s-polarized EL spectra, the optical dipole emission model of Setfos 4.6 software by Fluxim was used,[43] which implements a fit algorithm previously introduced and evaluated by Perucco et al.[20,21,25] and by Jenatsch et al.[44] The algorithm uses a superposition of deltalike emitters equally distributed inside the emission layer and adapts their height to minimize the difference between measured and simulated EL spectra and also extracts the PL spectrum of the emitter (cf. Figure 2a). The preferential horizontal alignment of the Ir(ppy)2(acac) emitter molecule was set to be 77% horizontal.[2,45] To calculate the exciton density from the measured radiative dipole density, the same radiative exciton decay rate as in the electrical OLED model was used. With this approach, the shape of the emission zone can be determined from optical measurements using a purely optical model.

Electrical OLED Model. The electrical simulations were performed with Setfos 4.6[43] software, which solves the drift-diffusion equations for electron and holes and considers exciton formation, diffusion, and decay in the framework of radiating dipoles inside a cavity including the Purcell effect.[22] Either constant or field-dependent electron and hole mobilities according to the Poole−Frenkel model with $\mu(E) = \mu_0\, e^{\gamma\sqrt{E}}$ were used.[22] The chosen HOMO/LUMO values are close to the ones displayed in Figure 1, and the boundary conditions for the charge carrier densities at the electrodes were set to satisfy the Fermi-level alignment at thermal equilibrium. Exciton generation is permitted only in the emission layer and follows the standard Langevin recombination.[20] Exciton recombination was modeled with a nonradiative decay rate of 0.09 μs^{-1} and a radiative decay rate of 0.63 μs^{-1}, resulting in a quantum efficiency of 87% and an exciton lifetime of 1.39 μs, as reported for similar systems.[3,46,47] The exciton diffusion coefficient was set to 63 nm^2/μs, which results in an exciton diffusion length of 9 nm, as observed in the optical measurements. If larger exciton diffusion coefficients were used, the exciton distribution inside the EML would smear out, and for very large values, the split emission zone can even disappear. The excitons were confined to the EML because the triplet energy of TCTA (2.8 eV)[48] is larger than that of Ir(ppy)$_2$(acac) (2.4 eV),[48] which prevents exciton transport into the HTL. The reported triplet energy for NBPhen (2.2 eV)[41] allows exciton transport into the ETL, but the exciton transport into the ETL is expected to be only a few percent[12] and was thus neglected. For emitters with high triplet energy levels, exciton transport should be considered. The organic−organic interfaces assume a quasi-Fermi-level alignment and use Boltzmann statistics to calculate the charge carrier densities in the OLED stack. For the results shown in Figures 7 and S2, exciton quenching was modeled as triplet−polaron quenching or triplet−triplet annihilation with quenching rate of 5×10^{-12} cm^3/s taken from refs 39 and 46.

ASSOCIATED CONTENT

Supporting Information

The Supporting Information is available free of charge on the ACS Publications website at DOI: 10.1021/acsami.8b09595.

Measured and simulated angle-dependent s-polarized EL spectra for constant current of 0.1 and 4 mA (Figure S1) and simulated transient EL decay and exciton density distribution for increased biases, considering triplet−triplet annihilation (Figure S2) (PDF)

AUTHOR INFORMATION

Corresponding Author

*E-mail: markus.regnat@zhaw.ch. Tel: +41 58 934 7346.

ORCID

Markus Regnat: 0000-0002-3485-3058

DOI: 10.1021/acsami.8b09595
ACS Appl. Mater. Interfaces 2018, 10, 31552−31559

Author Contributions

All authors contributed to the investigations and to the writing of the manuscript and have given approval to the final version of the manuscript.

Funding

Financial support from Samsung's Global Research Outreach (GRO) program and from the Swiss National Science Foundation under grant no. 162230 is gratefully appreciated.

Notes

The authors declare no competing financial interest.

■ ACKNOWLEDGMENTS

We thank L. Penninck, S. Altazin, and S. Jenatsch from Fluxim, T. Beierlein from ZHAW, and F. Nüesch from EPFL for fruitful discussions and valuable comments.

■ ABBREVIATIONS

EL, electroluminescence; EML, emission layer; EMZ, emission zone; ETL, electron transport layer; HOMO, highest occupied molecular orbital; HTL, hole transport layer; LUMO, lowest unoccupied molecular orbital; OLED, organic light-emitting diode; PL, photoluminescence; TPQ, triplet−polaron quenching; TTA, triplet-triplet annihilation

■ REFERENCES

(1) Kim, K.-H.; Lee, S.; Moon, C.-K.; Kim, S.-Y.; Park, Y.-S.; Lee, J.-H.; Woo Lee, J.; Huh, J.; You, Y.; Kim, J.-J. Phosphorescent Dye-Based Supramolecules for High-Efficiency Organic Light-Emitting Diodes. *Nat. Commun.* **2014**, *5*, No. 4769, DOI: 10.1038/ncomms5769.

(2) Kim, K.-H.; Moon, C.-K.; Lee, J.-H.; Kim, S.-Y.; Kim, J.-J. Highly Efficient Organic Light-Emitting Diodes with Phosphorescent Emitters Having High Quantum Yield and Horizontal Orientation of Transition Dipole Moments. *Adv. Mater.* **2014**, *26*, 3844−3847.

(3) Park, Y.-S.; Lee, S.; Kim, K.-H.; Kim, S.-Y.; Lee, J.-H.; Kim, J.-J. Exciplex-Forming Co-Host for Organic Light-Emitting Diodes with Ultimate Efficiency. *Adv. Funct. Mater.* **2013**, *23*, 4914−4920.

(4) Tanaka, D.; Sasabe, H.; Li, Y.-J.; Su, S.-J.; Takeda, T.; Kido, J. Ultra High Efficiency Green Organic Light-Emitting Devices. *Jpn. J. Appl. Phys.* **2007**, *46*, L10−L12.

(5) Udagawa, K.; Sasabe, H.; Cai, C.; Kido, J. Low-Driving-Voltage Blue Phosphorescent Organic Light-Emitting Devices with External Quantum Efficiency of 30%. *Adv. Mater.* **2014**, *26*, 5062−5066.

(6) Tsutsui, T.; Takada, N. Progress in Emission Efficiency of Organic Light-Emitting Diodes: Basic Understanding and Its Technical Application. *Jpn. J. Appl. Phys.* **2013**, *52*, No. 110001.

(7) Murawski, C.; Leo, K.; Gather, M. C. Efficiency Roll-Off in Organic Light-Emitting Diodes. *Adv. Mater.* **2013**, *25*, 6801−6827.

(8) Erickson, N. C.; Holmes, R. J. Investigating the Role of Emissive Layer Architecture on the Exciton Recombination Zone in Organic Light-Emitting Devices. *Adv. Funct. Mater.* **2013**, *23*, 5190−5198.

(9) Jeon, S. K.; Lee, J. Y. Direct Monitoring of Recombination Zone Shift during Lifetime Measurement of Phosphorescent Organic Light-Emitting Diodes. *J. Ind. Eng. Chem.* **2015**, *32*, 332−335.

(10) Jesuraj, P. J.; Hafeez, H.; Kim, D. H.; Lee, J. C.; Lee, W. H.; Choi, D. K.; Kim, C. H.; Song, M.; Kim, C. S.; Ryu, S. Y. Recombination Zone Control without Sensing Layer and the Exciton Confinement in Green Phosphorescent OLEDs by Excluding Interface Energy Transfer. *J. Phys. Chem. C* **2018**, *122*, 2951−2958.

(11) Ruhstaller, B.; Beierlein, T.; Riel, H.; Karg, S.; Scott, J. C.; Riess, W. Simulating Electronic and Optical Processes in Multilayer Organic Light-Emitting Devices. *IEEE J. Sel. Top. Quantum Electron.* **2003**, *9*, 723−731.

(12) Coburn, C.; Lee, J.; Forrest, S. R. Charge Balance and Exciton Confinement in Phosphorescent Organic Light Emitting Diodes. *Adv. Opt. Mater.* **2016**, *4*, 889−895.

(13) Sim, B.; Moon, C.-K.; Kim, K.-H.; Kim, J.-J. Quantitative Analysis of the Efficiency of OLEDs. *ACS Appl. Mater. Interfaces* **2016**, *8*, 33010−33018.

(14) Aminaka, E.; Tsutsui, T.; Saito, S. Effect of Layered Structures on the Location of Emissive Regions in Organic Electroluminescent Devices. *J. Appl. Phys.* **1996**, *79*, 8808−8815.

(15) Li, C.; Tsuboi, T.; Huang, W. Recombination Zone in Organic Light Emitting Diodes with Emitting Layer of Diphenylanthracene-Derivative Host. *Phys. Procedia* **2011**, *14*, 213−216.

(16) Zhang, Y.; Lee, J.; Forrest, S. R. Tenfold Increase in the Lifetime of Blue Phosphorescent Organic Light-Emitting Diodes. *Nat. Commun.* **2014**, *5*, No. 5008.

(17) Beierlein, T. A.; Ruhstaller, B.; Gundlach, D. J.; Riel, H.; Karg, S.; Rost, C.; Rieß, W. Investigation of Internal Processes in Organic Light-Emitting Devices Using Thin Sensing Layers. *Synth. Met.* **2003**, *138*, 213−221.

(18) van Eersel, H.; Bobbert, P. A.; Janssen, R. A. J.; Coehoorn, R. Monte Carlo Study of Efficiency Roll-off of Phosphorescent Organic Light-Emitting Diodes: Evidence for Dominant Role of Triplet-Polaron Quenching. *Appl. Phys. Lett.* **2014**, *105*, No. 143303.

(19) Mesta, M.; Carvelli, M.; de Vries, R. J.; van Eersel, H.; van der Holst, J. J. M.; Schober, M.; Furno, M.; Lüssem, B.; Leo, K.; Loebl, P.; Coehoorn, R.; Bobbert, P. A. Molecular-Scale Simulation of Electroluminescence in a Multilayer White Organic Light-Emitting Diode. *Nat. Mater.* **2013**, *12*, 652−658.

(20) Perucco, B.; Reinke, N. A.; Rezzonico, D.; Knapp, E.; Harkema, S.; Ruhstaller, B. On the Exciton Profile in OLEDs-Seamless Optical and Electrical Modeling. *Org. Electron.* **2012**, *13*, 1827−1835.

(21) Perucco, B.; Reinke, N. A.; Müller, F.; Rezzonico, D.; Ruhstaller, B. In *The Influence of the Optical Environment on the Shape of the Emission Profile and Methods of Its Determination*, Proceedings of SPIE, 2010; Vol. *7722*, p 77220F1.

(22) Ruhstaller, B.; Knapp, E.; Perucco, B.; Reinke, N.; Rezzonico, D.; Müller, F. Advanced Numerical Simulation of Organic Light-Emitting Devices. In *Optoelectronic Devices and Properties*; Sergiyenko, O., Ed.; Intech, 2011.

(23) van Eersel, H.; Bobbert, P. A.; Janssen, R. A. J.; Coehoorn, R. Effect of Förster-Mediated Triplet-Polaron Quenching and Triplet-Triplet Annihilation on the Efficiency Roll-off of Organic Light-Emitting Diodes. *J. Appl. Phys.* **2016**, *119*, No. 163102.

(24) van Mensfoort, S. L. M.; Carvelli, M.; Megens, M.; Wehenkel, D.; Bartyzel, M.; Greiner, H.; Janssen, R. A. J.; Coehoorn, R. Measuring the Light Emission Profile in Organic Light-Emitting Diodes with Nanometre Spatial Resolution. *Nat. Photonics* **2010**, *4*, 329−335.

(25) Perucco, B.; Reinke, N. A.; Rezzonico, D.; Moos, M.; Ruhstaller, B. Analysis of the Emission Profile in Organic Light-Emitting Devices. *Opt. Express* **2010**, *18*, A246−A260.

(26) Flämmich, M.; Gather, M. C.; Danz, N.; Michaelis, D.; Bräuer, A. H.; Meerholz, K.; Tünnermann, A. Orientation of Emissive Dipoles in OLEDs: Quantitative in Situ Analysis. *Org. Electron.* **2010**, *11*, 1039−1046.

(27) Danz, N.; Flämmich, M.; Setz, D. S.; Krummacher, B. C.; Michaelis, D.; Dobbertin, T. Detection of Sub-10 Nm Emission Profile Features in Organic Light-Emitting Diodes Using Destructive Interference. *Opt. Lett.* **2012**, *37*, 4134−4136.

(28) Mac Ciarnain, R.; Michaelis, D.; Wehlus, T.; Rausch, A. F.; Danz, N.; Bräuer, A.; Tünnermann, A. Emission from Outside of the Emission Layer in State-of-the-Art Phosphorescent Organic Light-Emitting Diodes. *Org. Electron.* **2017**, *44*, 115−119.

(29) Carvelli, M.; Janssen, R. A. J.; Coehoorn, R. Spatial Resolution of Methods for Measuring the Light-Emission Profile in Organic Light-Emitting Diodes. *J. Appl. Phys.* **2011**, *110*, No. 084512.

(30) Flämmich, M.; Michaelis, D.; Danz, N. In Situ Measurement of Spectrum, Emission Zone, and Dipole Emitter Orientation in OLEDs. *Proc. SPIE* **2011**, *7954*, No. 7954101.

(31) Flämmich, M.; Michaelis, D.; Danz, N. Accessing OLED Emitter Properties by Radiation Pattern Analyses. *Org. Electron.* **2011**, *12*, 83−91.

DOI: 10.1021/acsami.8b09595
ACS Appl. Mater. Interfaces 2018, 10, 31552−31559

(32) Coehoorn, R.; van Eersel, H.; Bobbert, P.; Janssen, R. Kinetic Monte Carlo Study of the Sensitivity of OLED Efficiency and Lifetime to Materials Parameters. *Adv. Funct. Mater.* **2015**, *25*, 2024−2037.
(33) Song, D.; Zhao, S.; Luo, Y.; Aziz, H. Causes of Efficiency Roll-off in Phosphorescent Organic Light Emitting Devices: Triplet-Triplet Annihilation versus Triplet-Polaron Quenching. *Appl. Phys. Lett.* **2010**, *97* (24), 243304.
(34) Reineke, S.; Lindner, F.; Huang, Q.; Schwartz, G.; Walzer, K.; Leo, K. Measuring Carrier Mobility in Conventional Multilayer Organic Light Emitting Devices by Delayed Exciton Generation. *Phys. Status Solidi B* **2008**, *245* (5), 804−809.
(35) Bhansali, U. S.; Jia, H.; Lopez, M. A. Q.; Gnade, B. E.; Chen, W.-H.; Omary, M. A. Controlling the Carrier Recombination Zone for Improved Color Stability in a Two-Dopant Fluorophore/Phosphor White Organic Light-Emitting Diode. *Appl. Phys. Lett.* **2009**, *94*, No. 203501.
(36) Lee, W. H.; Kim, D. H.; Jesuraj, P. J.; Hafeez, H.; Lee, J. C.; Choi, D. K.; Bae, T.-S.; Yu, S. M.; Song, M.; Kim, C. S.; Ryu, S. Y. Improvement of Charge Balance, Recombination Zone Confinement, and Low Efficiency Roll-off in Green Phosphorescent OLEDs by Altering Electron Transport Layer Thickness. *Mater. Res. Express* **2018**, *5*, No. 076201.
(37) Parshin, M. A.; Ollevier, J.; Van der Auweraer, M. Charge Carrier Mobility in CBP Films Doped with $Ir(ppy)_3$. *Proceedings of SPIE*, 2006; Vol. *6192*, p 61922A.
(38) Lee, S.-B.; Yasuda, T.; Yang, M.-J.; Fujita, K.; Tsutsui, T. Charge Carrier Mobility in Vacuum-Sublimed Dye Films for Light-Emitting Diodes Studied by the Time-of-Flight Technique. *Mol. Cryst. Liq. Cryst.* **2003**, *405*, 67−73.
(39) Reineke, S.; Walzer, K.; Leo, K. Triplet-Exciton Quenching in Organic Phosphorescent Light-Emitting Diodes with Ir-Based Emitters. *Phys. Rev. B* **2007**, *75*, No. 125328.
(40) Zhang, D.; Li, W.; Chu, B.; Zhu, J.; Li, T.; Han, L.; Bi, D.; Li, X.; Yang, D.; Yan, F.; Liu, H.; Wang, D.; Tsuboi, T. Low Efficiency Roll off at High Current Densities in Ir-Complex Based Electrophosphorescence Diode with Exciton Diffusing and Fluorescence Compensating Layers. *Appl. Phys. Lett.* **2007**, *91*, No. 183516.
(41) Yamazaki, S.; Tsutsui, T. *Physics and Technology of Crystalline Oxide Semiconductor CAAC-IGZO: Application to Displays*; John Wiley & Sons, 2017; p 252.
(42) Fluxim. *Platform for All-in-One Characterization of Solar Cells and OLEDs*, software version Paios 3.3. https://www.fluxim.com.
(43) Fluxim. *Setfos*, version 4.6. https://www.fluxim.com.
(44) Jenatsch, S.; Regnat, M.; Hany, R.; Diethelm, M.; Nüesch, F.; Ruhstaller, B. Time-Dependent p−i−n Structure and Emission Zone in Sandwich-Type Light-Emitting Electrochemical Cells. *ACS Photonics* **2018**, *5*, 1591−1598.
(45) Liehm, P.; Murawski, C.; Furno, M.; Lüssem, B.; Leo, K.; Gather, M. C. Comparing the Emissive Dipole Orientation of Two Similar Phosphorescent Green Emitter Molecules in Highly Efficient Organic Light-Emitting Diodes. *Appl. Phys. Lett.* **2012**, *101*, No. 253304.
(46) Kalinowski, J.; Stampor, W.; Mężyk, J.; Cocchi, M.; Virgili, D.; Fattori, V.; Di Marco, P. Quenching Effects in Organic Electrophosphorescence. *Phys. Rev. B* **2002**, *66*, No. 235321.
(47) Wehrmeister, S.; Jäger, L.; Wehlus, T.; Rausch, A. F.; Reusch, T. C. G.; Schmidt, T. D.; Brütting, W. Combined Electrical and Optical Analysis of the Efficiency Roll-Off in Phosphorescent Organic Light-Emitting Diodes. *Phys. Rev. Appl.* **2015**, *3*, No. 024008.
(48) Sun, N.; Wang, Q.; Zhao, Y.; Chen, Y.; Yang, D.; Zhao, F.; Chen, J.; Ma, D. High-Performance Hybrid White Organic Light-Emitting Devices without Interlayer between Fluorescent and Phosphorescent Emissive Regions. *Adv. Mater.* **2014**, *26*, 1617−1621.

DOI: 10.1021/acsami.8b09595
ACS Appl. Mater. Interfaces 2018, 10, 31552−31559